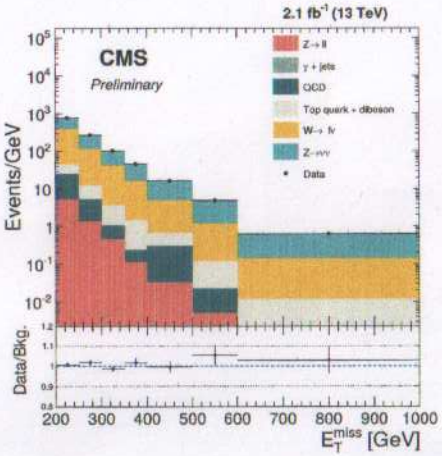

Figure 5.5: The missing transverse energy distribution after applying the described event selection, for data and MC.

5.4 Background estimation

The dominant background comes from events with a Z boson produced together with a number of jets, where the Z boson decays to two neutrinos. This produces the same signature of jets with missing energy as the signal, and results in an irreducible background. The second largest background consists of W + jets events with a leptonically decaying W boson. This background is already suppressed by the lepton veto, but a fraction of these events remain when the lepton is either not identified or outside of the detector acceptance. The remaining background events come from top quark decays, which are suppressed by the b-jet veto, semileptonic diboson (WW, WZ, and ZZ) decays, and QCD multijet events. The two main background contributions are estimated from five control regions in data consisting of dimuon, dielectron, single muon, single electron, and photon + jets events. The contributions from top quark decays and semileptonic diboson decays are estimated using simulated samples, while the QCD multijet background is estimated using a data-driven approach.

5.4.1 The Z and W background estimation

The traditional control region for the Z boson background is the dimuon control region. This region is dominated by $Z \to \mu\mu$ events, which are very similar to the $Z(\nu\nu)$ + jets background events, the only difference being the decay mode. The production mode and kinematics in the control region are very similar, as well as the acceptance. However, the branching ratio of the Z boson into two muons is 6 times smaller than the branching ratio to two neutrinos. As a result, the dimuon control region contains about 10 times less Z boson events than the signal region. In order to improve this statistical limitation, other control regions have been added as well.

The yield of $Z(\nu\nu)$ and $W(l\nu)$ + jets events in the signal region is therefore estimated from five control regions by using the ratio between data and MC in the control region, per bin of the hadronic recoil distribution. For the prediction using $Z \to \mu\mu$ events in the dimuon control region for example,

the predicted yield of $Z \to \nu\nu$ events is given by

$$N_{Z(\nu\nu)} = \frac{N^{data}_{Z(\mu\mu)}}{N^{MC}_{Z(\mu\mu)}} N^{MC}_{Z(\nu\nu)} \quad (5.1)$$

$$= \frac{N^{data}_{\mu\mu} - N_{Bkgd}}{N^{MC}_{Z(\mu\mu)}} N^{MC}_{Z(\nu\nu)} \quad (5.2)$$

$$= \frac{N^{data}_{\mu\mu} - N_{Bkgd}}{N^{MC}_{Z(\mu\mu)}} R_{Z(\mu\mu)\to Z(\nu\nu)} N^{MC}_{Z(\mu\mu)}, \quad (5.3)$$

where the number of $Z(\mu\mu)$ + jets events in data $N^{data}_{Z(\mu\mu)}$ is given by the number events in the dimuon sample, removing the number of background events, and $N^{MC}_{Z(\mu\mu/\nu\nu)}$ represent the number of $Z(\mu\mu/\nu\nu)$ + jets events in MC. The transfer factors, denoted by R, are derived from simulation and take into account the impact of lepton acceptance and efficiency, as well as the additional E_T^{miss} requirement for the single electron control region. They also include the difference in branching ratio and the relation between the differential cross sections of the photon, W, and Z boson production as a function of the boson p_T. The transfer factors are computed as a function of the hadronic recoil, and are shown for the five different control regions in Figure 5.6. Furthermore, the Z/W ratio shown in the bottom right plot of Figure 5.6 provides an additional constraint since the single lepton control regions are also used to estimate the $Z(\nu\nu)$ + jets background.

The simulated samples used for the background estimation are generated at leading order (LO) using the MADGRAPH generator, and corrected to next-to-leading order (NLO). These corrections are crucial in order correctly represent the data, since the simulation is approximately 40% higher than the data when using only LO calculations. The NLO QCD k-factors are derived from samples generated at NLO with MADGRAPH5_aMC@NLO, while the electroweak k-factors are obtained from theoretical calculations [130–133]. The differential cross section as a function of the boson p_T is shown in Figure 5.7 for photon, W, and Z production, and the obtained k-factors are displayed in the ratio plots. More details on the different control regions are given in the following.

Dimuon control region
In the dimuon control region the events are selected using the monojet triggers and applying the same requirements as described in Section 5.3 for the signal region, using the hadronic recoil instead of the missing transverse energy, except for the muon veto. Additionally, exactly two muons with opposite charge should be identified using the loose identification, and at least one should also pass the tight selection requirements. The leading muon should have a transverse momentum larger than 20 GeV, and the second one should have $p_T > 10$ GeV. Finally, the dimuon mass should be between 60 and 120 GeV, corresponding to the Z boson mass.

Single muon control region
In order to model the second largest background, coming from $W(l\nu)$ + jets events, a single muon control region is used. This control region is in addition also used to constrain the $Z(\nu\nu)$ + jets background. The events in the single muon control region are required to pass the monojet triggers and event selection replacing the E_T^{miss} by the hadronic recoil obtained by removing the muon, except for the muon veto. One muon should then pass the tight selection requirements and have $p_T > 20$ GeV.

Dielectron control region
The dielectron control region is also used to constrain the $Z \to \nu\nu$ background. The events are selected by the single electron triggers. Similarly to the dimuon control region, the events are required to pass the monojet selection, except for the electron veto. Instead, exactly two electrons with $p_T > 10$ GeV are required to pass the loose identification described in Section 4.3.3. In addition, at least one electron should pass the tight selection requirements, and the leading electron is required to have $p_T > 40$ GeV in order to be consistent with the single electron trigger. Finally, the dielectron mass should be between 60 and 120 GeV, in order to be consistent with a Z boson

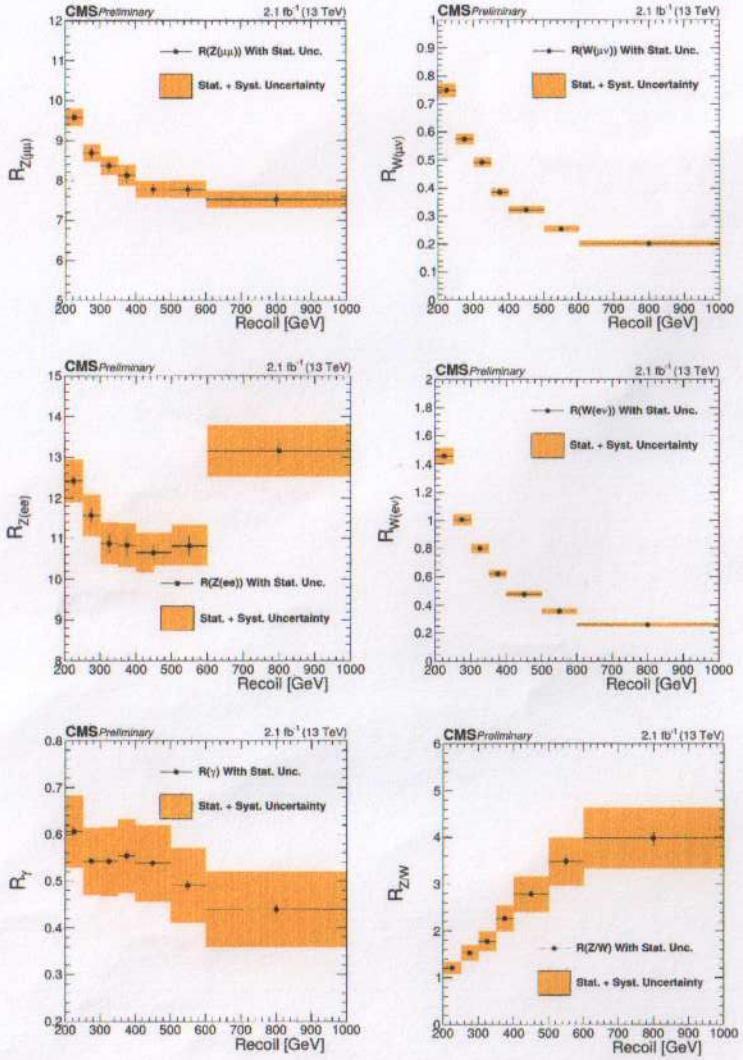

Figure 5.6: Transfer factors for the dimuon (top left), single muon (top right), dielectron (middle left), single electron (middle right), and photon + jets (bottom left) control regions. The ratio of the Z and W transfer factors is shown in the bottom right plot.

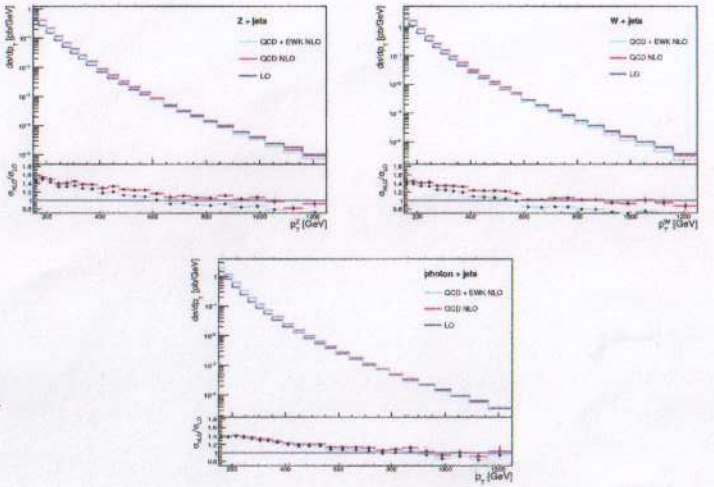

Figure 5.7: The differential cross section as a function of the boson p_T for photon, W,and Z production, using boson p_T-binned NLO samples. The resulting k-factors are shown in the ratio plots.

decay. The jump that can be observed in the last bin of the resulting transfer factor in the middle left plot of Figure 5.6 is due to the isolation requirement of the single electron trigger. This was verified by removing the trigger selection in MC, yielding a flat transfer factor.

Single electron control region

The single electron control region is used to constrain the $W(l\nu)$ + jets background. In the single electron control region, the events are required to have one electron with $p_T > 40$ GeV passing the tight selection requirements, analogous to the single muon control region. In this region, a large amount of QCD background is however present due to jets being wrongly reconstructed as electrons (is this correct?). In order to reject most of those events, an additional cut on the E_T^{miss}, which includes the single electron, is added at 50 GeV. This reduces the QCD background by an order of magnitude.

Photon + jets control region

Due to its large yield, the photon + jets control region provides the dominant constraint on the high-p_T part of the $Z(\nu\nu)$ + jets background. The selection of these events is done using the single photon triggers and applying the monojet selection, except for the photon veto. One photon is then required to pass the tight identification and to have $p_T > 175$ GeV. Additionally, it should be reconstructed inside the ECAL barrel ($|\eta| < 1.4442$) in order to achieve a high purity of at least 95%. Events with more than one photon passing the loose identification requirements described in Section 4.3.3 are rejected.

5.4.2 The QCD background estimation

While QCD multijet background events are generally well balanced in the transverse plane, missing transverse energy can arise in the event due to jet energy mismeasurements, punch-through, uninstrumented or defective regions in the detector, hot spots, or neutrinos from decays of heavy-flavour mesons. Although these effects are very rare, the QCD production cross section is very large compared to other processes,

and some events can be selected at high missing transverse energy. The event selection detailed in Section 5.3 was designed to suppress contributions from the QCD multijet background, reducing it to the percent level. However, this background is not well reproduced in the simulation, and thus requires a background estimation using a data control region.

The yield is predicted by combining two different approaches, namely the "rebalance and smear" technique and the $\Delta\phi$ extrapolation method. The rebalance and smear technique minimises the missing transverse energy through a kinematic fit using the jet resolutions. The event is then rebalanced by varying each jet and the remaining hadronic recoil within their computed uncertainties. The resulting jets are then smeared with the measured jet resolution, and the prediction for the QCD E_T^{miss} distribution is obtained. The used data for this method are selected based on jets and applying a cut on the H_T present in the event. For the $\Delta\phi$ extrapolation method, the QCD background is estimated in data selected using the signal triggers and applying the events selection, but inverting the $\Delta\phi$ selection cut and instead requiring $\min\Delta\phi(jet, E_T^{miss}) < 0.5$. An extrapolation is then made to the signal region using transfer factors derived from simulated events generated at LO with MADGRAPH in several bins of H_T. The obtained estimation using this method yields a contribution that is a factor 2 larger than the prediction from simulation, ~~which agrees well with the the rebalance and smear technique~~ as can be seen in Figure 5.8.

this is not used in the analysis. Phil tried but gave up. It was never completed, and ATC didn't care.

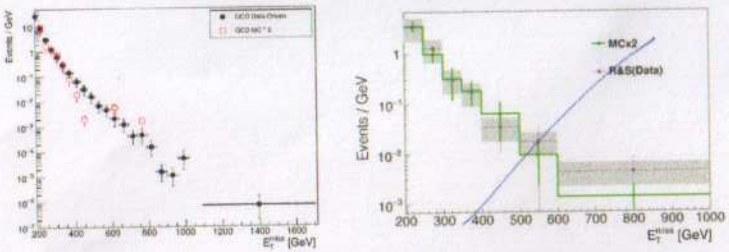

Figure 5.8: Predicted E_T^{miss} distribution of the QCD multijet background obtained using the $\Delta\phi$ extrapolation method (~~left~~) ~~and the rebalance and smear technique~~ (right), using data (black) and MC simulations (red). The simulation is scaled by a factor 2.

5.4.3 Simulation-based background estimation

Contributions are also expected from diboson production, from top quark decays, both from $t\bar{t}$ and single top production, and from $Z(ll)$ + jets events where the leptons are not detected. These backgrounds are estimated from MC simulations.

Top quarks typically decay into a W boson and a b quark. When the W boson decays leptonically, a neutrino is produced, generating genuine missing transverse energy. If the event is not removed by the b-jet veto and the lepton is not identified, this type of events contributes to the background in the signal region. However, due to the small production cross section and the applied event selection, only a small fraction of these events are selected. In order to estimate the contribution of this background, a $t\bar{t}$ sample has been produced at LO with MADGRAPH, and single top events were generated with POWHEG at NLO.

When one of the weak bosons produced in diboson events decays leptonically, generating one or more neutrinos, and the other one decays hadronically, jets and missing transverse energy are produced. The samples used to estimate this background have been produced using PYTHIA.

Finally, when the leptons in $Z(ll)$ + jets events are lost or out of the detector acceptance, these events can mimic the monojet signature as well. MC samples have been generated at LO using MADGRAPH in several bins of H_T in order to estimate the contribution from this sub-dominant background.

you need somewhere here the ~~reference~~ citation to these NLO EWK corrections

5.5 Systematic uncertainties

For the main backgrounds, multiple systematic uncertainties on the transfer factors are taken into account. Systematic uncertainties are added for the muon efficiency, the electron efficiency, the lepton veto, the photon efficiency, and the photon purity in the photon + jets sample.

Uncertainties are also added from theory, to take into account variations of the factorisation and renormalisation scales, PDF uncertainties, and the NLO electroweak corrections. The former 3 uncertainties are shown in Figure 5.9 for the Z + jets, W + jets, and photon + jets samples. The uncertainties are then propagated to the transfer factors, and are displayed in Figure 5.10. To evaluate the PDF uncertainty, the samples are reweighted with event-by-event scale factors representing the shift in the kinematic distributions from variations in the PDF. The transfer factors are then produced for each variation, and the RMS of the variation is taken as PDF uncertainty. Similarly, the renormalisation and factorisation scales are varied up and down by a factor 2, and the uncertainties are derived from the resulting transfer factors. For the electroweak corrections, the full correction is taken as an uncertainty.

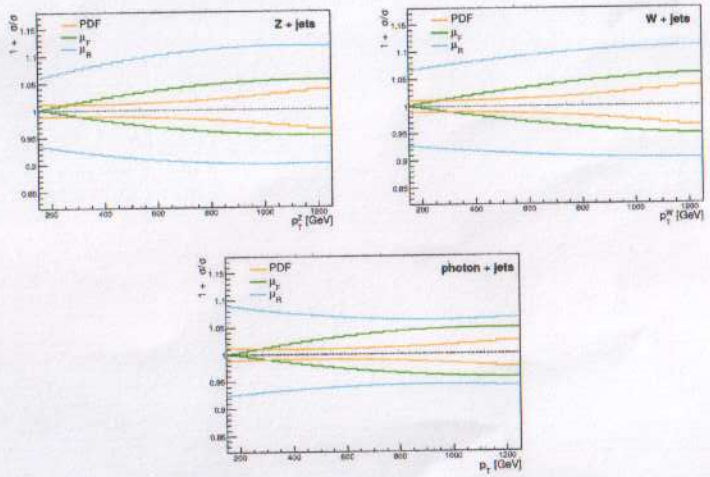

Figure 5.9: The PDF, renormalisation, and factorisation scale uncertainties for the Z + jets (top left), W + jets (top right), and photon + jets (bottom) samples. The uncertainties from the renormalisation and factorisation scales are obtained by separately varying them up and down by a factor 2.

For the remaining sub-dominant backgrounds, systematic uncertainties are included to take into account the uncertainties from the jet energy scale and the jet energy resolution of the jets. Additionally, systematic uncertainties of 10%, 29%, and 50% are added to account for the uncertainty on the production cross section of the top, diboson, and QCD processes, respectively. For the top quark background, a systematic uncertainty of 4% is included as well, due to the uncertainty on the b-tagging applied for the b-jet veto. Finally, a systematic uncertainty of 5.5% is added for all backgrounds derived from MC simulations, to take into account the uncertainty on the luminosity measurement.

Lastly, for the signal models described in Section 2.2.4 and simulated as summarised in Section 4.1.1, systematic uncertainties are included for the luminosity and to take into account the uncertainties from the jet energy scale and the jet energy resolution. The systematic uncertainties coming from variations of the factorisation and renormalisation scales and PDF uncertainties amount to 20% for the vector and axial signal samples and 30% for the scalar and pseudoscalar signals.

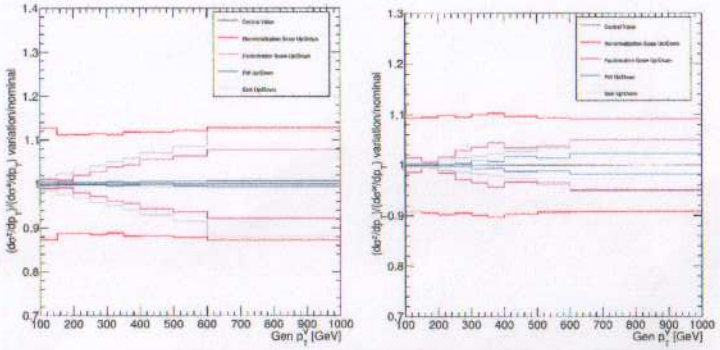

Figure 5.10: The theoretical uncertainties on the Z/γ (left) and Z/W (right) transfer factors.

5.6 Results

The results are extracted by performing a binned fit to the missing energy spectrum, fitting simultaneously over the five control regions and the signal region, under a given signal hypothesis. This is done using the CL_S criterion [134, 135], using the asymptotic approximation of the test statistic distributions implemented in the RooStat-based Combine tool and modelling the systematic uncertainties described in Section 5.5 as nuisance parameters. The nuisance parameter uncertainties are propagated as shape and normalization variations of the $Z(\nu\nu)$ + jets and $W(l\nu)$ + jets background. In Figure 5.11, the nuisance parameters and their uncertainties are shown before and after the fit to the data in the control regions. Before the fit they are all centred at 0 and have an uncertainty of 1. After the fit, the two largest pulls originate from the statistical uncertainty on the Z/W transfer factor and the uncertainty on the muon scale factor, but no significant tension is present in the fit and most nuisance parameters are not pulled or constrained by the fit.

Figures 5.12 and 5.13 show the hadronic recoil distributions in the different control regions, before and after the fit. The photon + jets control region, which has the largest yields, drives the fit and the post-fit prediction therefore corresponds well to the data. A good agreement is observed in all control regions, and the overall change in the transfer factors is less than 10%.

Table 5.1 gives the background prediction for the various background processes in bins of hadronic recoil, using a background-only fit. Correspondingly, the fit under the background-only hypothesis is shown in Figure 5.14 and a good agreement is observed between the data and the prediction. The uncertainty on the hadronic recoil is below 10% for all bins.

Process	E_T^{miss} $[200-250]$ GeV	E_T^{miss} $[250-300]$ GeV	E_T^{miss} $[300-350]$ GeV	E_T^{miss} $[350-400]$ GeV	E_T^{miss} $[400-500]$ GeV	E_T^{miss} $[500-600]$ GeV	E_T^{miss} $[>600]$ GeV
$Z(\nu\nu)$ + jets	19521	7473	3085	1447	1126	350	184
$W(l\nu)$ + jets	15422	4793	1728	650	428	104	47.9
$Z(ll)$ + jets	259	67	22.4	5.1	3.0	0.44	0.12
Top	715	240	73.8	32.5	18.3	2.9	2.5
Dibosons	148	38	8.2	2.3	0.61	0.66	0.07
QCD	773	346	157	77	64	19.5	15.8
Total	36837 ± 246	12958 ± 115	5075 ± 63	2214 ± 38	1639 ± 33	478 ± 14	250 ± 12
Observed	36858	13010	4981	2248	1614	484	260

Table 5.1: Post-fit background predictions in the signal region and observed yield. The predictions and uncertainties are obtained from the background-only simultaneous fit in the signal and control regions.

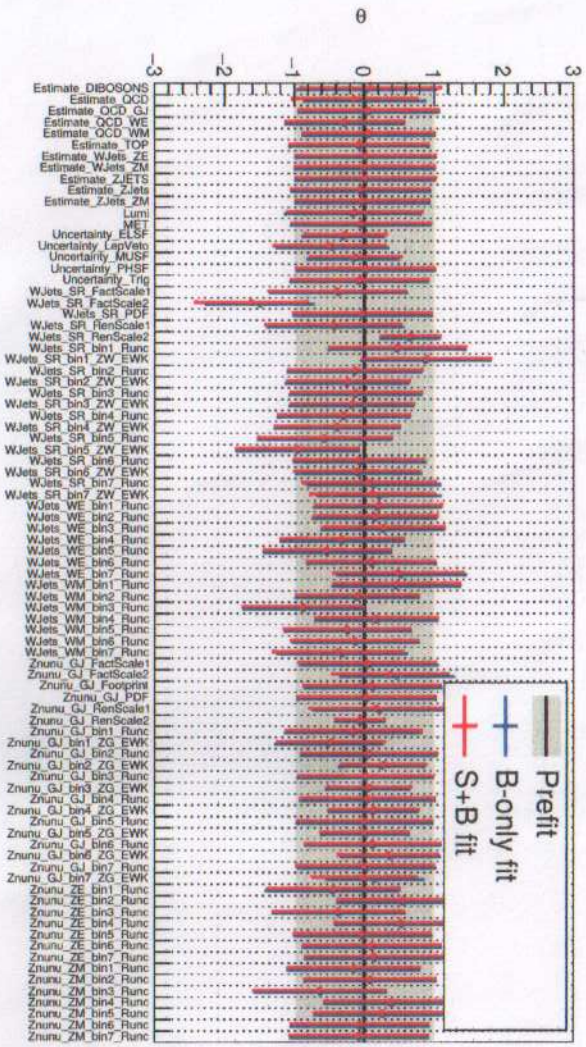

Figure 5.11: The post-fit nuisance parameters and their uncertainties, compared to the pre-fit values.

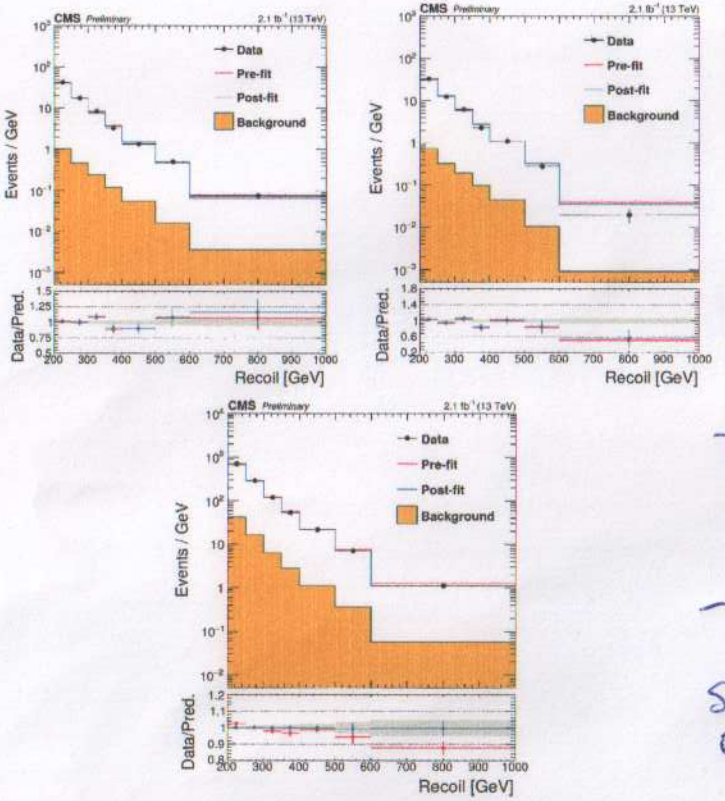

Figure 5.12: Comparison between data and prediction before (pre-fit) and after (post-fit) the simultaneous fit to the different control regions, in the dimuon (left), dielectron (right) and photon + jets (bottom) control regions. The grey band shows the uncertainty per bin, including all relevant systematic uncertainties.

5.7 Improvements going from the 2015 to 2016 analysis

Several iterations of the monojet analysis were performed during Run 2 in 2015 and 2016, improving the achieved sensitivity with the increase in available data and additional developments to the analysis strategy, and adding new interpretations. In 2015, a first analysis with data at a centre-of-mass energy of 13 TeV was carried out [136], using data corresponding to an integrated luminosity of 2.1 fb^{-1}. In this first iteration of the search, the NLO k-factors applied to correct the LO samples used for the estimation of the background from Z and W bosons are derived from inclusive NLO samples, which are not binned in boson p_T. These k-factors are shown in Figure 5.15, and can be compared to the k-factors obtained from p_T-binned samples used in the following iterations of the analysis and shown in Figure 5.7.

In 2016, the analysis was extended to the mono-V channel [137], which can give rise to a monojet-like signature. At high p_T, the production of a W or Z boson which decays hadronically, can be effectively reconstructed as a single jet of large cone radius. However, in this chapter the focus is on the monojet channel and the added improvements during 2016. For this analysis, data collected in 2015 was used, corresponding to 2.3 fb^{-1}. The used NLO k-factors were derived using the p_T-binned samples, as described in Section 5.4.1. This contribution was a first step in the improvements added to the analysis.

A substantial difference in the next iteration of the 2016 analysis [65] is the increase in collected data, which allowed to reduce the statistical uncertainties and set stronger limits on the considered models. For these results, data collected in the first half of 2016 and corresponding to an integrated luminosity of 12.9 fb^{-1} were available. One of the improvements that were added is the direct use of MC samples generated at leading order for the estimation of the main backgrounds. This was possible by generating samples that are binned in W boson p_T. As a result of this second contribution to the improvement of the background prediction, no k-factors need to be applied to the W + jets sample and no additional systematic uncertainties are to be introduced for this. Figures 5.16 and 5.17 show the obtained reduction in the overall post-fit uncertainty on the predictions in the 5 control regions.

5.8 Interpretation

The results of the second iteration of this search, using the mono-V final state as well, are interpreted in terms of simplified dark matter models assuming a vector, axial-vector, scalar, or pseudoscalar mediator decaying to a pair of fermionic dark matter particles, as described in Section 2.2.4. As no significant excess was observed, upper limits are placed 95% confidence level (CL) on the ratio of the signal cross section to the predicted cross section, $\mu = \sigma/\sigma_{th}$. These limits are shown as a function of the mediator mass (m_{med}) and the dark matter mass (m_{DM}) in Figures 5.18 and 5.19, for the four types of mediators. The regions where the 95% CL upper limits on μ are less than one are considered to be excluded.

For the vector and axial-vector models, mediator masses up to 1.95 TeV are excluded, while mediator masses up to 100 GeV and 430 GeV can be excluded for the scalar and pseudoscalar models, respectively. Figures 5.18 and 5.19 also show the constraint from the observed cosmological relic density of dark matter, which was determined from the WMAP and Planck CMB measurements. The expected dark matter abundance is estimated using a thermal freeze-out mechanism and compared to the observed cold dark matter density, assuming that the considered dark matter candidate is the dominant component of the observed dark matter.

The obtained limits can also be translated into 90% CL upper limits on the dark matter-nucleon scattering cross section $\sigma_{\text{SI/SD}}$, in order to compare them to results from direct detection experiments. The exclusion contours in the $m_{\text{DM}} - \sigma_{\text{SI/SD}}$ plane are obtained following the approaches outlined in [138–140], where σ_{SI} stands for spin-independent and σ_{SD} for spin-dependent dark matter-nucleon cross section. The resulting limits are shown in Figures 5.20 and 5.21.

For the vector and scalar mediators, the 90% CL upper limits on the spin-independent cross section are compared to results from the CDMSLite [141], LUX [142], PandaX-II [143], and CRESST-II [144] experiments. This shows that monojet limits are complementary to the results from the direct detection experiments at low dark matter masses. The 90% CL upper limits on the spin-dependent cross section obtained for the axial-vector mediator are compared to the PICO-2L [145], PICO-60 [146], IceCube [147],